Cross-linked cellulose beads as an eco-friendly support for ZnO/SnO2/carbon xerogel hybrid photocatalyst: Exploring the synergy between adsorption and photocatalysis under simulated sunlight

Nicolas Perciani de Moraes, Renan Amarante Pereira, Thiago Vieira Chicuta da Silva, Bruno Henrique Baena da Silva, Gabrielle Policarpo de Assis, Tiago Moreira Bastos Campos, Gilmar Patrocínio Thim, Marcos Roberto de Vasconcelos Lanza, Larissa de Freitas, Liana Alvares Rodrigues

PII: S0141-8130(23)04725-6

DOI: https://doi.org/10.1016/j.ijbiomac.2023.127826

Reference: BIOMAC 127826

To appear in: *International Journal of Biological Macromolecules*

Received date: 24 August 2023

Revised date: 3 October 2023

Accepted date: 23 October 2023

Please cite this article as: N.P. de Moraes, R.A. Pereira, T.V.C. da Silva, et al., Cross-linked cellulose beads as an eco-friendly support for ZnO/SnO2/carbon xerogel hybrid photocatalyst: Exploring the synergy between adsorption and photocatalysis under simulated sunlight, *International Journal of Biological Macromolecules* (2023), https://doi.org/10.1016/j.ijbiomac.2023.127826

Cross-linked cellulose beads as an eco-friendly support for ZnO/SnO_2/carbon xerogel hybrid photocatalyst: exploring the synergy between adsorption and photocatalysis under simulated sunlight

Nicolas Perciani de Moraes[1], Renan Amarante Pereira[2], Thiago Vieira Chicuta da Silva[2], Bruno Henrique Baena da Silva[2], Gabrielle Policarpo de Assis[2], Tiago Moreira Bastos Campos[3], Gilmar Patrocínio Thim[3], Marcos Roberto de Vasconcelos Lanza[1], Larissa de Freitas[2], Liana Alvares Rodrigues[2*]

1 - São Carlos Institute of Chemistry, University of São Paulo, Av. Trab. São Carlense, 400 - Parque Arnold Schimidt, São Carlos - SP, 13566-590

2 - Lorena School of Engineering- EEL/USP, Estrada Municipal do Campinho S/N, CEP 12602-810, Lorena, São Paulo, Brazil

3- Aeronautics Institute of Technology - ITA/CTA, Praça Mal. Eduardo Gomes 50, CEP 12228-900, São José dos Campos, São Paulo, Brazil.

*Corresponding authors: liana.r@usp.br

Abstract

This paper explores the application of cross-linked cellulose beads as a sustainable and cost-effective support for the ZnO/SnO_2/carbon xerogel hybrid photocatalyst. The application of the developed photocatalytic beads, named CB-Cat, was directed at a simultaneous adsorption/photocatalysis process, which was carried out under simulated sunlight. The characterization of the CB-Cat indicated a good dispersion of the photocatalyst of choice throughout the cellulose matrix, confirming its incorporation into the cellulose beads. Furthermore, it is possible to observe the presence of the photocatalyst on the surface of the CB-Cat, confirming its availability for the photonic activation process. The results showed that the simultaneous adsorption/photocatalysis process was optimal for enhancing the efficiency of methylene blue (MB) removal, especially when compared to the isolated adsorption process. Additionally, the regeneration of the CB-Cat between cycles was favorable toward the maintenance of the MB removal efficiency, as the process carried out without regeneration displayed significant efficiency drops between cycles. Finally, the mechanism evaluation evidenced that hydroxyl and superoxide radicals were the main responsible for the MB photocatalytic degradation during illumination with simulated sunlight.

Keywords: *Cellulose beads; adsorption/photocatalysis synergy; water treatment*

1. Introduction

In the context of environmental preservation, heterogeneous photocatalysis has recently emerged as a pioneering strategy for tackling the daunting challenge of remediating organic pollutants derived from industrial discharges, as these molecules pose significant threats to ecosystems and human health [1,2]. This advanced oxidative process utilizes specialized semiconductor materials to initiate photochemical reactions upon exposure to light; these catalysts generate electron-hole pairs that drive a series of oxidation and reduction reactions, breaking down complex organic molecules into simpler, less harmful compounds such as carbon dioxide and water [3,4]. This intrinsic ability to mineralize a wide range of organic pollutants, including persistent and toxic substances, has positioned photocatalytic processes as highly promising tools for contaminated water remediation.

Additionally, the application of heterogeneous photocatalysis can be highlighted due to its efficiency, versatility, and environmental compatibility. Unlike traditional methods that often produce secondary pollutants or require extensive energy inputs, photocatalysis is able to harness solar energy as the driving force, making it a sustainable and clean approach [5]. However, challenges persist for its efficient application in large-scale industrial processing plants. In liquid-phase photocatalytic systems, one of the primary challenges is the separation of fine photocatalyst particles from the treated solution [6]. Conventional separation methods such as filtration and sedimentation might be inadequate due to the small particle sizes and potential aggregation of catalysts [7]. Therefore, innovative separation techniques and material designs play a crucial role in realizing the full potential of this technology for sustainable environmental remediation.

From this perspective, the use of supported photocatalysts for the degradation of organic contaminants can offer various advantages in the sustainable and cost-effective use of photocatalysts, enhancing the viability of the proposed photocatalytic process. This strategy allows

for the utilization of continuously operated treatment systems, eliminating the necessity for intricate solid/liquid separation methods [8,9]. Ceramics, zeolites, and materials based on silica and carbon are among the most popular materials employed as supports for photocatalysts [10–12]. The ideal support for photocatalysts must meet the following criteria: robust bonding between the catalyst and support, considerable specific surface area, and good affinity for pollutant adsorption. In this context, cross-linked cellulose beads have emerged as a promising support for photocatalysts in recent years [13,14]. Cellulose is a cheap, abundant, and sustainable natural raw material, with excellent recyclability and biocompatibility. The preparation of cellulose beads through crosslinking reactions is reported as ideal for producing materials with high surface area, high stability, good mechanical resistance, and excellent adsorptive properties [15–17]. Moreover, the morphological and textural properties of the beads can be easily controlled through modifications to the synthesis conditions, allowing the generation of functional materials with a variety of distinct properties [18]. Thus, the immobilization of photocatalysts on this type of support is an interesting strategy, as its ideal intrinsic properties, low cost, and eco-friendly nature are expected to contribute positively toward the development of simpler and more efficient photocatalytic processes. Furthermore, considering the adsorptive properties of the cellulose beads, a synergic hybrid process between heterogeneous photocatalysis and adsorption can be achieved, which would be highly beneficial for effluent remediation.

Regarding the choice of efficient photocatalysts, photocatalysts with low charge recombination and visible light activity are on the center stage of novel and efficient photocatalytic processes [19]. Moraes et al. (2021) have recently developed the hybrid zinc oxide/tin(IV) oxide/carbon xerogel photocatalyst, which presented excellent activity for the degradation of 4-chlorophenol under visible light [20]. The elevated efficiency of the photocatalyst was achieved due to the facilitated charge transfer derived from the type-II heterojunctions developed between

semiconductors (ZnO/SnO_2), as well as by the inclusion of the carbon xerogel, which improved the morphological properties of the composite and functioned as a solid-state electron mediator [20].

Hence, this work will explore the application of cross-linked cellulose beads as a sustainable and cost-effective support for the ZnO/SnO_2/carbon xerogel hybrid photocatalyst, aiming at effluent treatment applications. To that intention, the removal of methylene blue was studied in a discontinuous system, intending to study the synergistic effect between adsorption and heterogeneous photocatalysis during the treatment process, which was conducted under simulated sunlight.

2. Materials and methods

2.1 Synthesis of the ZnO/SnO_2/carbon xerogel hybrid photocatalyst

The proposed hybrid photocatalyst was synthesized following the methodology proposed by Moraes et al. (2021) [20]. 8 g of zinc chloride ($ZnCl_2$, 97% w/w, CAS Nº 7646-85-7) and 0.072 g of tin chloride ($SnCl_2 \cdot 2H_2O$, 99% w/w, CAS Nº 10025-69-1) were dissolved in 50 mL of deionized water with magnetic stirring at room temperature. After the dissolution of the salts, 0.5 g of black-wattle tannin (Phenotan AP) was incorporated into the solution, still under magnetic stirring. The composite precipitation took place upon the addition of 10 g of potassium hydroxide (85% w/w, CAS Nº 1310-58-3), which had been previously dissolved in 50 mL of deionized water. The resulting precipitate underwent washing until the filtrate reached a pH of 7 and contained no trace of chloride ions. Subsequently, the material was dried in an oven at 100 °C for 24 hours and then sifted through a 325-mesh sieve for particle size refinement. Finally, the composite was added to a closed crucible and calcined within a muffle furnace at 300 °C for 30 minutes, operating under a nitrogen atmosphere (0.5 L min^{-1}) and with a heating rate of 10 °C per minute.

2.2 Synthesis of the photocatalyst/microcrystalline cellulose beads

Initially, 12 g of urea (99% w/w, CAS Nº 57-13-6) and 7 g of sodium hydroxide (NaOH, 97% w/w, CAS Nº 1310-73-2) were added to a glass beaker. After that, 80 mL of deionized water was added, and the system was maintained under magnetic stirring until complete dissolution of the reactants was observed. Subsequently, 5 g of microcrystalline cellulose (MCC, 99% w/w, CAS Nº 9004-34-6) was added to the system, which was then maintained at the temperature of -10 ºC. After the complete solubilization of the MCC, 8 g of the synthesized photocatalyst was added to the solution, which was homogenized under magnetic stirring. Finally, a peristaltic pump was employed to add the prepared mixture to a sodium chloride coagulant solution (1.3 mol L^{-1}), under a drop-wise scheme. The coagulant solution, acting as a non-solvent, infiltrates the cellulose droplets, resulting in the formation of physical cross-linking networks due to the self-association forces among cellulose macromolecules. The replacement of the solvent with a non-solvent induces the desolvation of cellulose molecules and promotes the restoration of intra and inter-molecular hydrogen bonds, thereby enhancing the stability of the cellulose bead's structure [21]. The beads obtained were then dried in an oven for 24 h (100º C) and washed with deionized water until no yellowish coloration was observed in the filtrate. The beads containing the immobilized photocatalyst will be identified as CB-Cat in the manuscript. Figure 1 shows a scheme of the synthesis process of the CB-Cat.

Figure 1 – Visual representation of the mechanism of coagulation and formation of the CB-Cat.

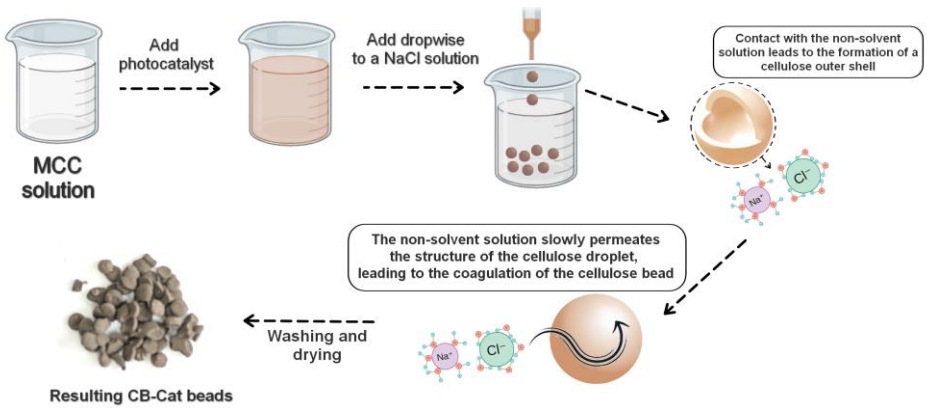

2.3 Characterization

The beads obtained in Section 2.2 were characterized using the following techniques:

- X-ray diffractometry: A PANalytical Empyrean Alpha diffractometer was utilized, utilizing copper X-ray radiation, within the range of 10-70º (step size of 0.013º and scan speed of 0.06 s per step).
- Infrared spectroscopy: Fourier transform infrared spectroscopy (FTIR) was performed using a PerkinElmer Frontier spectrometer equipped with a universal attenuated total reflectance sensor (UATR). The FTIR analysis covered the spectral range of 450 to 4000 cm^{-1}.
- Scanning electron microscopy and energy dispersive spectroscopy: The micrographs were obtained in a TESCAN Vega 3 XMU microscope with an energy dispersive spectroscopy (EDS) module.
- Diffuse reflectance spectroscopy: To obtain the diffuse reflectance spectra of the samples, a Shimadzu UV-2600 spectrophotometer equipped with an integrating sphere attachment was employed.
- Nitrogen adsorption-desorption isotherms: A V-Sorb 2800 equipment (Gold APP) was employed in this analysis. The samples underwent pretreatment at 120 ºC for 2 hours under vacuum conditions. To determine the specific surface area, both the Brunauer–Emmett–Teller (BET) method and t-plot analysis were carried out. The total pore volume was estimated at a relative pressure of $P/P_0 = 0.99$. Additionally, the pore size distribution was determined using the non-local density functional theory (nLDFT).

2.4 Evaluation of methylene blue removal

All the tests proposed in this section were conducted in a jacketed batch reactor, with the following dimensions: 10 cm of internal diameter and 10 cm of height. For each test, 500 mL of 25 mg L^{-1} methylene blue (MB) solution was added to the proposed reactor. The cellulose beads

(CB-Cat) were added to a metallic mesh support, which was inserted inside the reactor. The system was maintained under magnetic stirring and the temperature was controlled through the passage of cooling water by the reactor's jacket. The lamp used to simulate sunlight was an OSRAM Ultra Vitalux (300 W, 1950 $\mu mol_{photons}\, m^{-2}\, s^{-1}$) [22]. Figure 2 shows a representation of the reactor.

Figure 2 – Scheme of the reactor employed in the tests

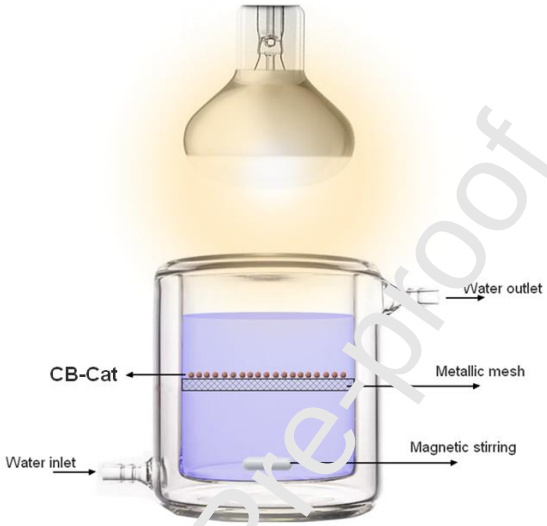

In order to understand the synergistic effects taking place between the adsorption and photocatalysis processes, the tests of methylene blue removal were conducted under three different operational modes, as described below:

i) Simultaneous adsorption/photocatalysis, with regeneration of the CB-Cat between cycles: In these tests, the CB-Cat used was regenerated between each cycle of MB removal. To that intention, the beads were added to an ethanol solution (250 mL), in which they were kept for 24 h. The simple adsorption process was also performed in order to compare its results with the hybrid adsorption/photocatalysis process.

ii) Simultaneous adsorption/photocatalysis, without regeneration of the CB-Cat between cycles: In these tests, the CB-Cat used was not regenerated between each cycle of MB removal. As described in the previous item, simple adsorption tests were also performed in this case.

iii) Separated adsorption/photocatalysis: In these tests, the system was maintained without light irradiation until the adsorption-desorption equilibrium was obtained. After that, light

irradiation was turned on and the photocatalytic process was initiated. For the photolysis test, after the adsorption-desorption process was concluded, the beads were removed from the reactional system and light irradiation was initiated.

For all tests, the concentration of methylene blue was defined spectrophotometrically, at the wavelength of 673 nm. To that intention, 1 mL aliquots were collected throughout the experiment, at pre-defined time intervals. To evaluate the mechanism involved in the generation of active radicals and degradation of MB, scavenger probing tests were performed (following the methodology proposed in item iii). The following scavengers were employed: potassium chromate (1 mmol, electron scavenger), isopropanol (5% v/v, hydroxyl radical scavenger), benzoquinone (1 mmol, superoxide radical scavenger), and EDTA (1 mmol, electron-hole scavenger) [23,24].

3. Results and discussions

3.1 Characterization

Figure 3 shows the results of the X-ray diffractometry of the CB-Cat.

Figure 3 – X-ray diffractogram of the CB-Cat material

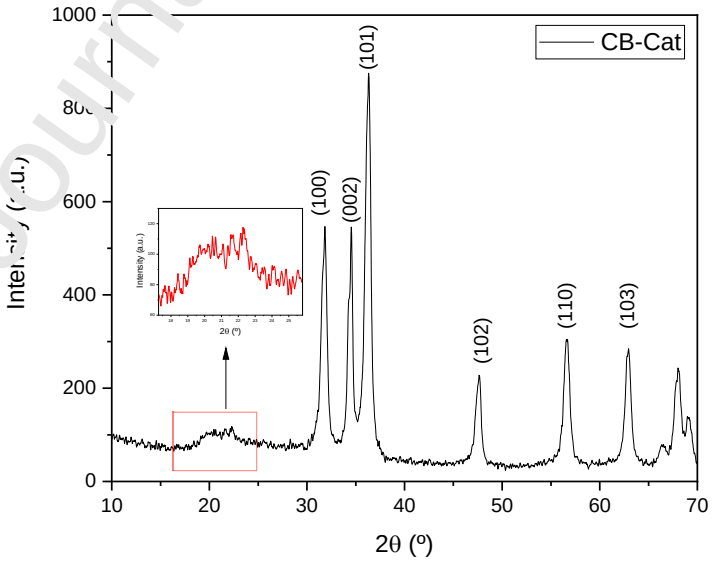

Firstly, it is possible to identify that the hexagonal structure of the zinc oxide is present in the beads produced. The peaks related to this structure can be identified at the angles 2θ of: 31.7 (100), 34.3 (002), 36.4 (101), 47.6 (102), 56.6 (110), 62.9 (103), and 66.4 ° (200) [23]. This

demonstrates the incorporation of the synthesized photocatalyst into the cellulose beads, as desired. Furthermore, the detail in Figure 3 shows the presence of two peaks with lesser intensity in the diffractogram of the CB-Cat sample. These crystalline peaks, located at $2\theta = 20.2$ and 22.5, correspond to the (1 1 0) and (2 0 0) lattice planes, respectively, of the cellulose type-II structure [25]. Finally, the peaks related to SnO_2 could not be identified in the diffractogram due to its low mass fraction in the photocatalyst developed, which is expected to be 1%.

Figure 4 shows the scanning electron micrographs of both the CB-Cat and photocatalyst developed.

Figure 4 – Scanning electron micrographs of the: A) Photocatalyst (50000x); B) CB-Cat (85x); C) CB-Cat (500x); D) CB-Cat (5000x); E) CB-Cat (20000x); F) CB-Cat (50000x)

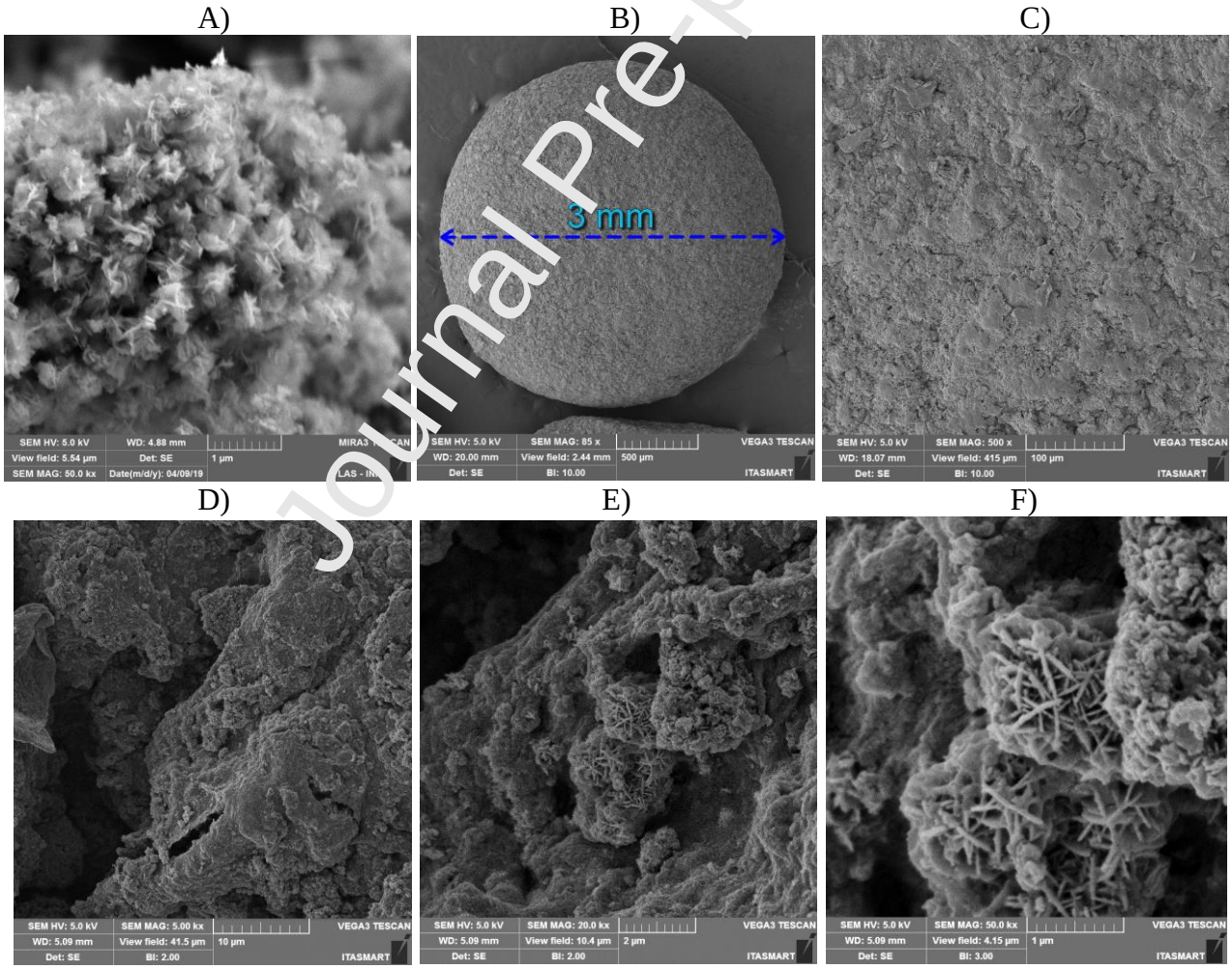

Firstly, Figure 4A shows that the photocatalyst developed is composed of plate-like particles, as reported by Moraes et al. (2021) in their previous work [20]. Figure 4B evidences the spherical nature of the cellulose beads produced in this work, with an approximate diameter of 3 mm, while Figures 4C and 4D show that the surface of the CB-Cat has a rugged and porous nature. Further magnification (Figures 4E and 4F) reveals the existence of plate-like particles embedded at the CB-Cat's surface, indicating that the photocatalyst is available to propagate the photocatalytic mechanism during the remediation process proposed in this work. Furthermore, the related literature reports that materials composed of particles with well-defined edges, such as the ones observed for the photocatalyst employed, are optimal for photocatalytic applications due to the significant presence of superficial defects, which can act toward the separation of the photogenerated charges [26].

Figure 5 shows the elemental mapping of both the photocatalyst and the CB-Cat beads, as obtained by energy dispersive spectroscopy.

Figure 5 – A) Elemental mapping of the CB-Cat cellulose beads; B) Elemental mapping of the photocatalyst

A)

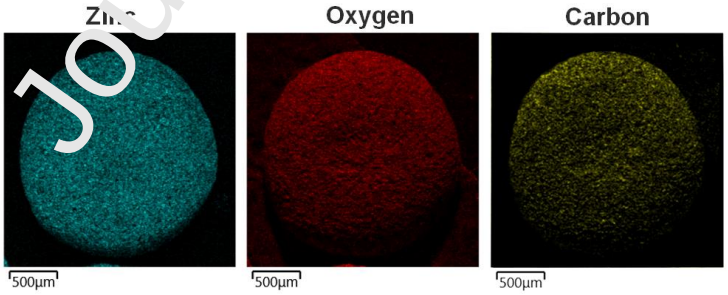

B)

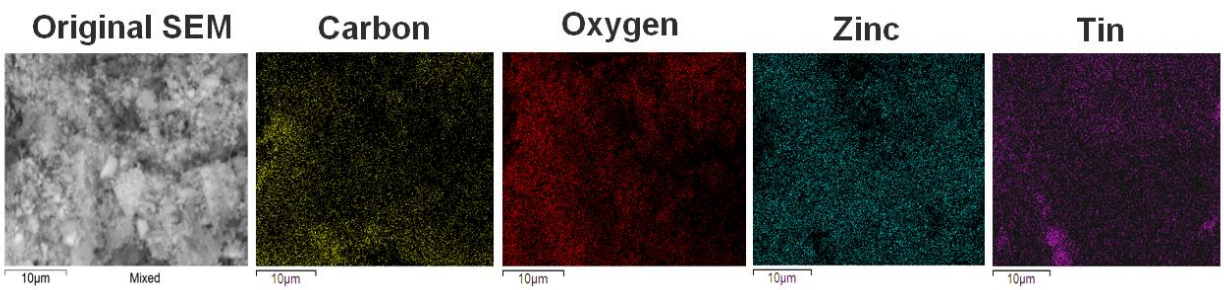

The elemental mapping obtained for the CB-Cat confirms the presence of the developed photocatalyst throughout the entire surface of the developed photoactive cellulose beads, as evidenced by the Zinc distribution shown in Figure 5A. Hence, this result confirms the excellent dispersibility of the photocatalyst employed in this work and the homogenous structure of the composite beads. In this context, the catalytic performance of this kind of composite is influenced not only by the size and nature of the deposited nanoparticles but also by their distribution; thus, the homogeneous dispersion of the photocatalyst on the supporting cellulose material is favorable towards elevated catalytic activity. Additionally, the elemental mapping of the photocatalyst confirms the presence of the tin element throughout its surface (Figure 5B).

Figure 6 shows the nitrogen adsorption-desorption isotherm of the CB-Cat, along with the pore diameter distribution plot.

Figure 6 – A) Nitrogen adsorption-desorption isotherm for the CB-Cat; B) Pore diameter distribution for the CB-Cat

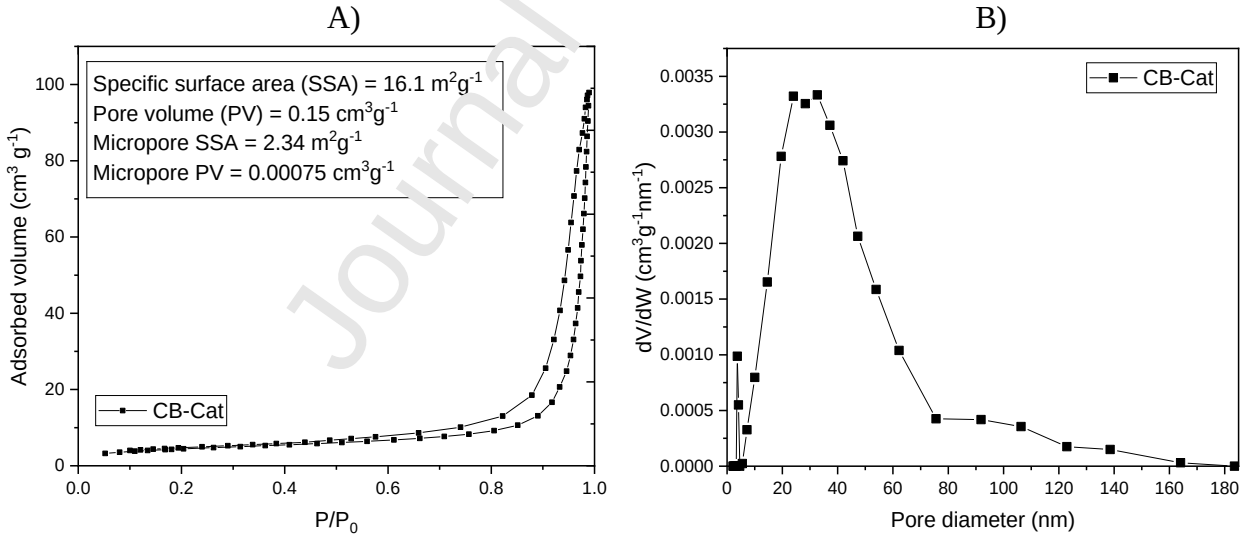

According to the criteria established by the International Union of Pure and Applied Chemistry, Figure 6A demonstrates that the nitrogen adsorption-desorption isotherm conforms to a Type IV classification, with an H3 hysteresis loop [27,28]. This observation suggests that the material in question is predominantly mesoporous and possesses pores with a slit-like configuration [24]. The parameters obtained from the BET and t-plot methods corroborate this theory, with a

specific surface area of 16.1 $m^2 g^{-1}$ and a micropore area of only 2.34 $m^2 g^{-1}$. Additionally, the pore distribution plot indicates that the CB-Cat is composed mainly of mesopores in the range of 10-80 nm, which is beneficial for the proposed process, as the methylene blue molecule to be employed is 1.447 nm in length [29]. It is worth pointing out that the photocatalyst employed possesses a specific surface area of 15.47 $m^2 g^{-1}$ in powdered form and an average pore size of approximately 25 nm, which is quite similar to the one found for the CB-Cat. Therefore, no loss of specific surface area was encountered by the immobilization of the photocatalyst on the cellulose beads, which is beneficial for the adsorption and photocatalytic degradation of the MB blue by the CB-Cat.

Figure 7 shows the infrared and diffuse reflectance spectrum for the CB-Cat sample.

Figure 7 – A) FTIR spectrum obtained for the CB-Cat sample; B) Diffuse reflectance spectrum of the CB-Cat sample

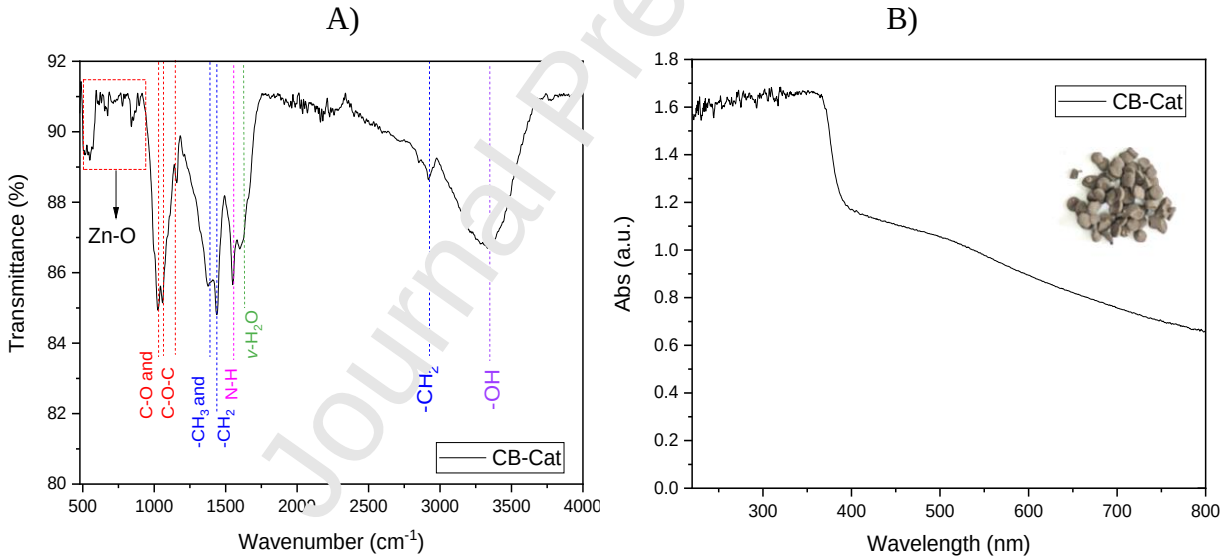

The infrared spectrum displayed in Figure 7A further confirms the incorporation of the photocatalyst into the cellulose beads. In the spectrum, the peaks located between 500 and 900 cm^{-1} can be related to the presence of the Zn-O bondings found in the structure of the photocatalyst [30]. On the other hand, the peaks at 1030, 1065 and 1150 cm^{-1} can be related to the C-O and C-O-C bondings present in the structure of the cellulose, while the peaks at 1390, 1450, and 2910 cm^{-1} are related to the C-H stretching of $–CH_2$ and $–CH_3$ groups [31,32]. Finally, the peaks at 1620 and

3300 cm^{-1} are related to the presence of hydroxyl groups, characteristic of adsorbed water, carboxyl, and phenolic groups, whereas the peak at 1540 cm^{-1} can be attributed to the presence of N-H bonds, probably derived from the use of urea during the synthesis pathway [33].

The diffuse reflectance spectrum of the CB-Cat can be divided into two major absorption regions. The first, located at wavelengths lower than 420 nm, is related to the absorption edge of the zinc oxide present in the photocatalyst, which is a characteristic behavior for this semiconductor. The second region, related to visible light absorption ($\lambda > 420$ nm), can be related to both the carbon xerogel present in the photocatalyst and the cellulose beads, as this absorption is commonly found in carbon-based materials [30].

Ghobadi has outlined a straightforward approach to ascertain the bandgap energy of a material by employing the Tauc relation (Equation 1) [23].

$$\left(\frac{Abs}{\lambda}\right)^{1/m} = B_1\left(\frac{1}{\lambda} - \frac{1}{\lambda_{gap}}\right) + B_2 \qquad (1)$$

In this context, "Abs" represents the absorption value linked to a specific wavelength, denoted as λ. The wavelength associated with the bandgap is labeled as λ_{gap}, while B_1 and B_2 stand for empirical constants. The transition factor, denoted as "m," holds a value of 0.5 in this scenario.

The reciprocal of λ_{gap} parameter can be ascertained through linear extrapolation of the data $\left(\frac{Abs}{\lambda}\right)^{1/m}$ vs $\frac{1}{\lambda}$ plot to $y = 0$. The energy bandgap can then be computed using the subsequent equation (Equation 2) [23].

$$E_{gap} = \frac{1240}{\lambda_{gap}} \qquad (2)$$

where E_{gap} symbolizes the bandgap energy (in electronvolts, eV), and λ_{gap} corresponds to its associated wavelength. A band gap approximately equal to 3.2 eV was found for the CB-Cat sample, which is the characteristic value of the zinc oxide's bandgap energy [34].

3.2 Methylene blue removal tests

Firstly, the adsorption capacity of the developed CB-Cat material was evaluated through the construction of an adsorption isotherm (Figure 8). The fitting of this isotherm was carried out utilizing the subsequent isotherm models: Langmuir (Equation 3), Freundlich (Equation 4), and Sips (Equation 5) [35–38]. The parameters obtained are displayed in Table 1.

$$\frac{C_e}{q_e} = \frac{1}{q_{max} k_L} + \frac{C_e}{q_{max}} \quad (3)$$

where q_{max} signifies the highest quantity of MB that the CB-Cat can adsorb (mg g^{-1}). q_e represents the adsorption capacity of MB at equilibrium (mg g^{-1}), C_e denotes the concentration of MB at the point of adsorption equilibrium (mg L^{-1}), and k_L stands for the Langmuir adsorption constant (L mg^{-1}).

$$q_e = k_F C_e^{\frac{1}{n}} \quad (4)$$

where k_F (L mg^{-1}) and $1/n$ are the constants characteristic of the Freundlich isotherm.

$$q_e = \frac{q_{max} k_s C_e^n}{1 + k_s C_e^n} \quad (5)$$

where n is the Sips model exponent, k_s is the Sips equilibrium constant (L mg^{-1})

Figure 8 – Methylene blue adsorption isotherm obtained for the CB-Cat

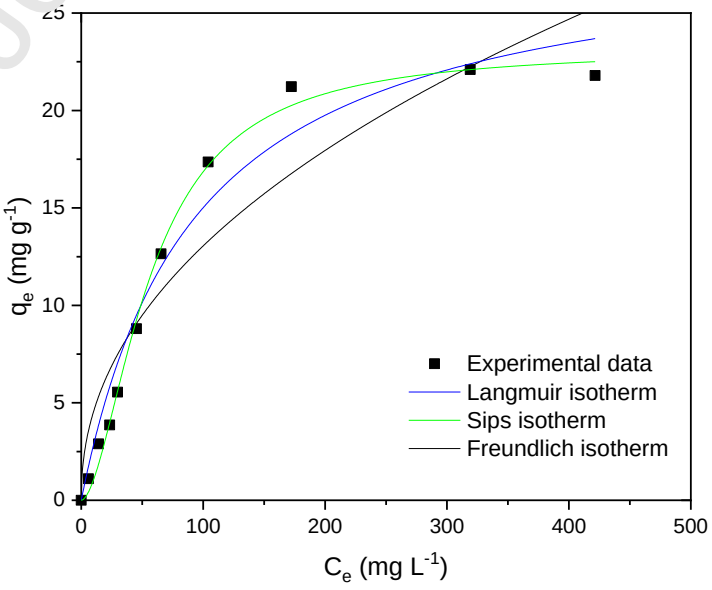

Table 1 – Parameters obtained using the proposed isotherm models

Langmuir isotherm			**Freundlich isotherm**		
q_{max} **(mg g^{-1})**	k_L (L mg^{-1})	R^2	k_F (L mg^{-1})	n	R^2
28.8	0.011	0.971	1.57	0.45	0.889

Sips isotherm			
q_{max} **(mg g^{-1})**	k_S (L mg^{-1})	n	R^2
23.2	0.00085	1.75	0.998

The results show that the Sips isotherm obtained the highest value of R^2 and, therefore, can be selected as the most appropriate model to describe the adsorption process evaluated. This model can be described as a 3-parameters hybrid model, which is an amalgamation of the Langmuir and Freundlich equations. Low adsorbate concentrations cause the model to converge towards the Freundlich isotherm, whereas high adsorbate concentrations result in a monolayer adsorption behavior in line with the Langmuir isotherm. Furthermore, if the *n* value is equal to 1, homogeneous adsorption is confirmed and the model converges to the Langmuir equation, even at low concentrations. Thus, this model can be used to describe a wide array of heterogeneous and homogeneous adsorption systems, circumventing the major limitations of both the Langmuir and Freundlich models. Considering the results obtained, the *n* value found for the Sips isotherm indicates that the surface of the CB-Cat leads to a heterogeneous adsorption process.

Following the study presented in Figure 8, the behavior of the CB-Cat for methylene blue removal was studied in the simultaneous adsorption/photocatalysis test with the regeneration of the photocatalytic beads between cycles, as proposed in Section 2.4. The results are shown in Figure 9.

Figure 9 – Simultaneous adsorption/photocatalysis tests, with regeneration between cycles: A) Adsorption only; B) Adsorption/photocatalysis test; C) Desorption results for the

adsorption tests; D) Desorption results for the simultaneous adsorption/desorption tests (C_0 = 25 mg L^{-1}, $m_{CB\text{-}Cat}$ = 1.8 g, V = 500 mL)

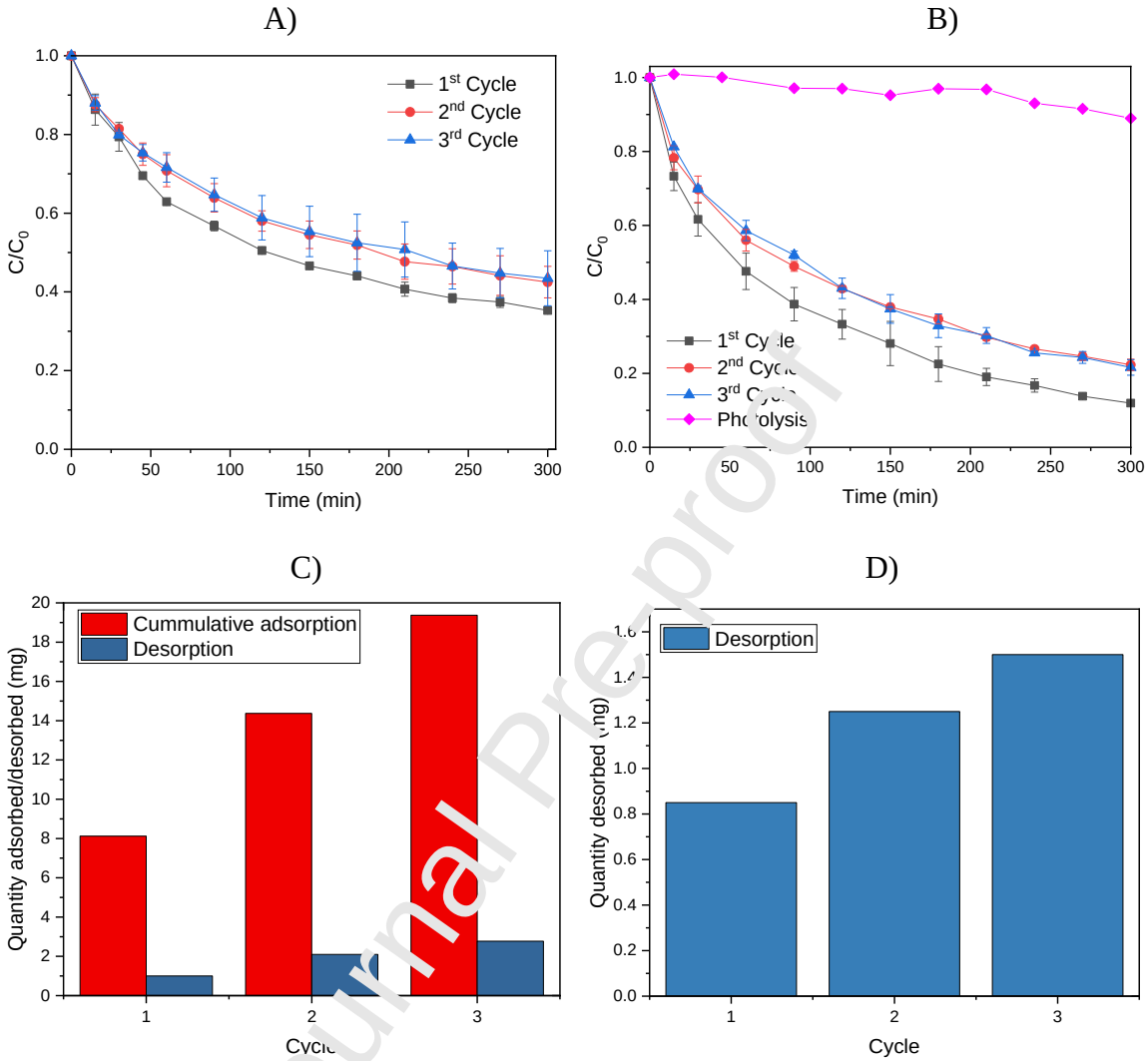

From the results exposed in Figure 9, two major conclusions can be drawn. First, the inclusion of the simulated sunlight during the experiment results in a significant boost for the MB removal in all cycles evaluated. As an example, a nearly 40% increase in methylene blue removal was observed for the simultaneous adsorption/photocatalysis test during the first cycle. Therefore, it is evident that the photocatalyst immobilized in the cellulose beads led to considerable photodegradation of the MB molecule, highlighting the synergy between the adsorption/photocatalysis processes. This is further evidenced by the photolysis test, which only obtained 10% removal efficiency for the MB, indicating that the immobilized photocatalyst played a major role in the MB removal obtained during the adsorption/photocatalysis test. Second, a drop

in the removal efficiency was observed between the first and second cycles for both the adsorption and adsorption/photocatalysis tests, in a similar manner and intensity. This drop can be explained by the fact that not all of the MB was removed during the regeneration of the CB-Cat between cycles, which would likely diminish the availability of adsorption sites after each cycle. However, it can also be noted that such a drop was not observed between the second and third cycles, indicating that regeneration of the CB-Cat counterbalanced the MB saturation process between these cycles.

Observing the results from the desorption procedure (Figures 9C and 9D), it can be seen that higher quantities of MB are desorbed after each cycle, which is consistent with the fact that, after each cycle, higher quantities of MB are adsorbed on the CB-Cat's surface. Additionally, it is possible to notice that the desorbed quantity of MB is lower in the simultaneous adsorption/photocatalysis tests, indicating that a part of the adsorbed methylene blue was further degraded through a direct photocatalysis mechanism.

In order to evaluate the results obtained in a kinetic manner, the following models were used: for the adsorption process, the pseudo-second-order model (Equation 6) was used, whereas, for the adsorption/photocatalysis process, a simplified Langmuir-Hinshelwood (L-H) kinetic model was employed (Equation 7) [39,40]. The results are shown in Table 2.

$$\frac{t}{q_t} = \frac{1}{k_2 q_e^2} + \frac{t}{q_e} \quad (6)$$

where qt and qe are the adsorbed amount of MB at a given time (t) and equilibrium, respectively, and k_2 is the rate constant of the pseudo-second-order adsorption model.

$$ln\left(\frac{C_0}{C}\right) = k_r K_{ad} t = k_{app} t \quad (7)$$

where C_0 represents the initial concentration of methylene blue and k_{app} is the apparent removal rate constant.

Table 2 – Kinetic parameters obtained from the experimental data

Cycle	Adsorption				Adsorption/photocatalysis		
	% Removed	q_e (mg g^{-1})	k_2 (g mg^{-1} min^{-1})	R^2	% Removed	k_{app} (min^{-1})	R^2
1	65	6.25	0.0022	0.997	88	0.0067	0.983
2	58	5.1	0.0023	0.995	78	0.0048	0.975
3	57	4.9	0.0024	0.996	78	0.0046	0.971
Photolysis	-	-	-	-	10	0.0004	0.976

The results show that the data obtained was in good agreement with the proposed models, as R^2 values reasonably close to 1 were found. Furthermore, a reduction in both the q_e and k_{app} values was obtained for the second cycle, which was expected due to the experimental data, as explained previously. Also, no major modification was observed between the second and third cycles, as expected.

Figure 10 shows the diffuse reflectance spectra and a visual illustration of the CB-Cat after the 3 cycles of MB removal.

Figure 10 – A) Diffuse reflectance spectra and a visual illustration of the CB-Cat after 3 cycles of MB removal, with regeneration; B) Scanning electron micrograph of the CB-Cat after 3 cycles of MB removal, with regeneration

A) B)

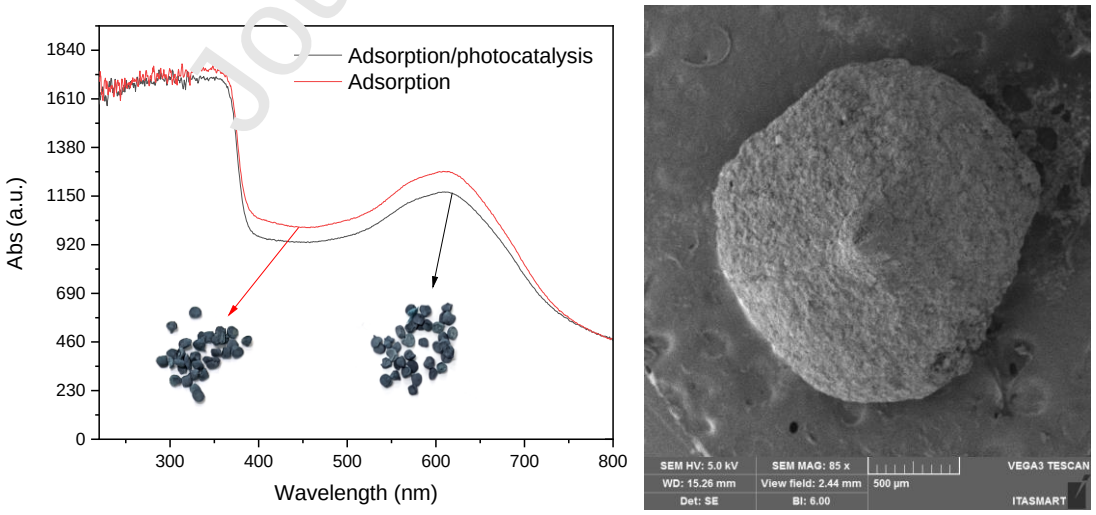

Analyzing Figure 10A, it is possible to identify a new absorption band on the CB-Cat spectra after the methylene blue removal process, which can be related to the methylene blue still

adsorbed on the surface of the beads. This notion is further corroborated by the blueish tint displayed by the beads. It is also possible to notice that the band is less intense in the material collected from the adsorption/photocatalysis process, indicating that this synergic process resulted in a lesser quantity of adsorbed methylene blue that remained after three cycles of adsorption/photodegradation, likely due to the photodegradation of adsorbed MB molecules. Furthermore, Figure 10B shows that the CB-Cat was able to maintain its bead-like structure after the 3 cycles of MB removal.

Figure 11 shows the study of the simultaneous adsorption/photocatalysis test without regeneration of the CB-Cat between cycles.

Figure 11 – Simultaneous adsorption/photocatalysis tests, without regeneration: A) Adsorption only; B) Adsorption/photocatalysis test (C_0 = 25 mg L^{-1}, $m_{CB\text{-}Cat}$ = 1.8 g, V = 500 mL)

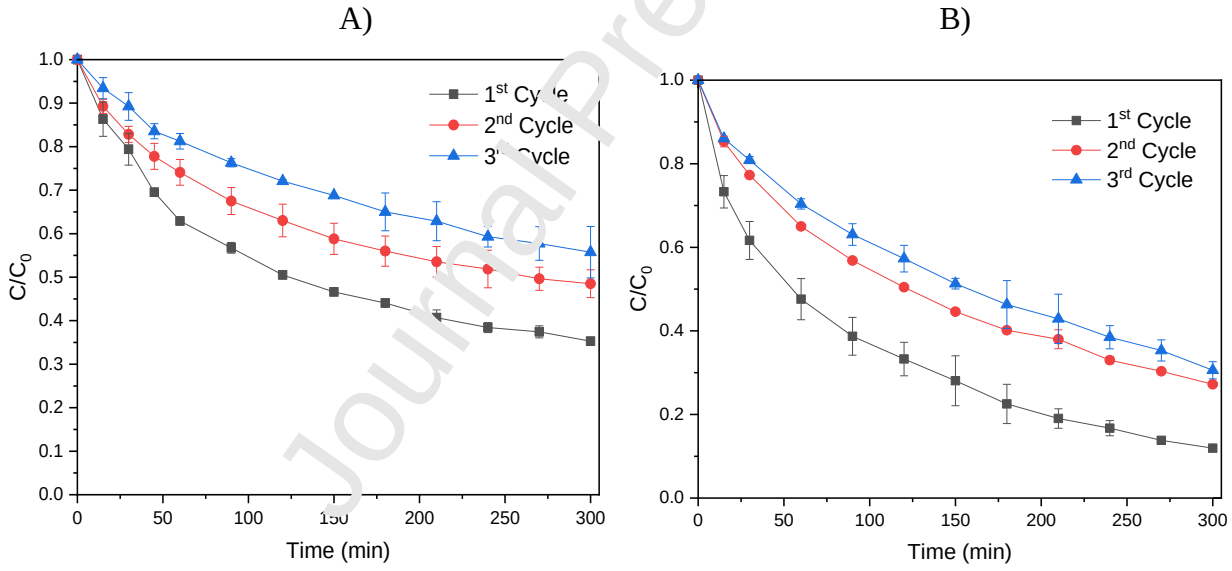

Figure 11 evidences that, without the regeneration between cycles, there is a progressive loss of removal efficiency when applying the CB-Cat under multiple cycles. As discussed previously, this is probably related to the saturation of adsorption sites by the methylene blue originating from previous cycles. Hence, without the regeneration process between cycles to counterbalance the MB accumulation, the results obtained can be taken as expected. Furthermore, since a higher quantity of adsorbed MB did not lead to an increased photodegradation rate, it can be

implied that the photodegradation of the MB occurs mostly through the indirect mechanism, which is dependent on the generation of active radicals, such as hydroxyl and superoxide radicals. It can also be implied that no dye-sensitization effect is being promoted by the adsorbed methylene blue onto the photocatalyst as, in this case, a higher amount of adsorbed MB would lead to a greater sensitization effect and increased photocatalytic efficiency [41].

The kinetic evaluation of the data was conducted in the same manner as proposed for the tests with regeneration. The results are shown in Table 3.

Table 3 – Kinetic parameters obtained from the experimental data (without regeneration between cycles)

	Adsorption				**Adsorption/photocatalysis**		
Cycle	% Removed	q_e (mg g^{-1})	k_2 (g mg^{-1} min^{-1})	R^2	% Removed	k_{app} (min^{-1})	R^2
1	65	6.25	0.0022	0.997	88	0.0067	0.983
2	52	4.5	0.0014	0.993	73	0.0041	0.979
3	45	4.0	0.0024	0.998	70	0.0036	0.990

Once again, the proposed models were a good fit for the experimental data, as indicated by the R^2 values obtained. The incremental decrease in the MB removal efficiency can be corroborated by the values of q_e and k_{app} derived from the experimental data, as expected.

Figure 12 shows the diffuse reflectance spectra of the CB-Cat after 3 cycles without regeneration, as well as a visual representation of the material.

Figure 12 – A) Diffuse reflectance spectra of the CB-Cat after 3 cycles, without regeneration; B) Scanning electron micrograph after 3 cycles, without regeneration

A) B)

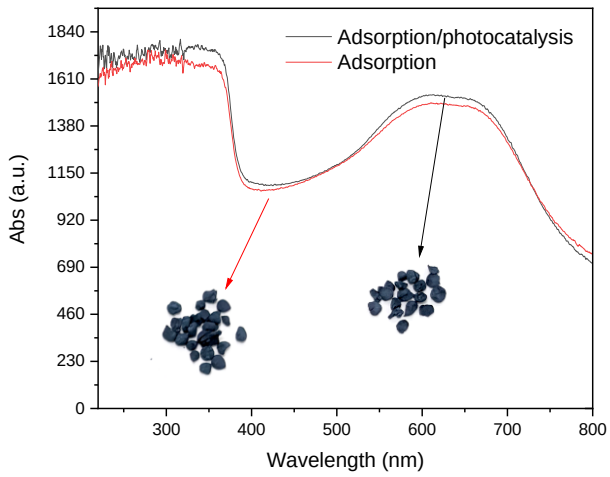

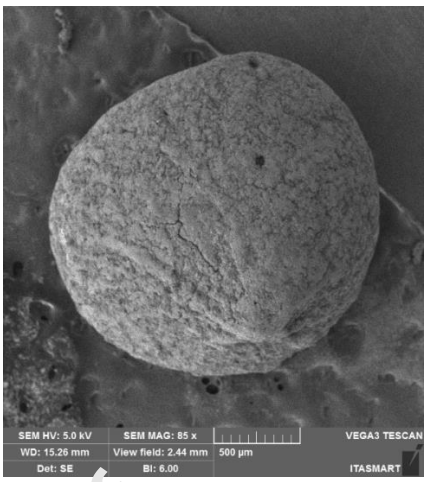

Observing Figure 12A, it can be noted that the absorption band of the adsorbed MB is much more intense than the one observed in Figure 10A, as no amounts of the adsorbed dye were removed between cycles through regeneration. This can be further verified by the coloration of the non-regenerated CB-Cat beads, which is much more intense and darker than the color observed previously for the regenerated beads. Therefore, it can be said that the regeneration process between cycles is favorable to the removal efficiency of the CB-Cat towards methylene blue, as the saturation of adsorption sites by the dye is hindered. Furthermore, it is noticeable that there is no major difference in the absorption spectrum of the CB-Cat after three cycles in the adsorption and adsorption/photocatalysis processes without regeneration. Thus, it can be implied that the regeneration of the CB-Cat after each cycle was favorable towards the photocatalytic efficiency of the employed catalytic beads. Additionally, the CB-Cat bead-like structure was also maintained after 3 cycles of reuse for the tests without regeneration.

Figure 13 shows the results obtained when applying the CB-Cat in the separated adsorption and photocatalysis process. To that intention, light irradiation was only initiated when the adsorption-desorption equilibrium was observed. Furthermore, in this case, the pseudo-first-order adsorption model (Equation 8) was also applied to verify if the model proposed previously is the more suitable option.

$$ln\,(q_e - q_t) = -k_1 t + lnq_e \quad (8)$$

where *qt* and *qe* are the adsorbed amount of MB at a given time (*t*) and equilibrium, respectively, and k_1 is the rate constant of the pseudo-first-order adsorption model.

Figure 13 – A) Adsorption of MB (24 h); B) Photocatalytic degradation of MB; C) Linear fitting of the adsorption data to the proposed models; D) Linear fitting of the photocatalysis data to the pseudo-first-order model (C_0 = 25 mg L^{-1}, $m_{CB\text{-}Cat}$ = 1.8 g, V = 500 mL); E) Impact of active radicals using the scavenger probing method

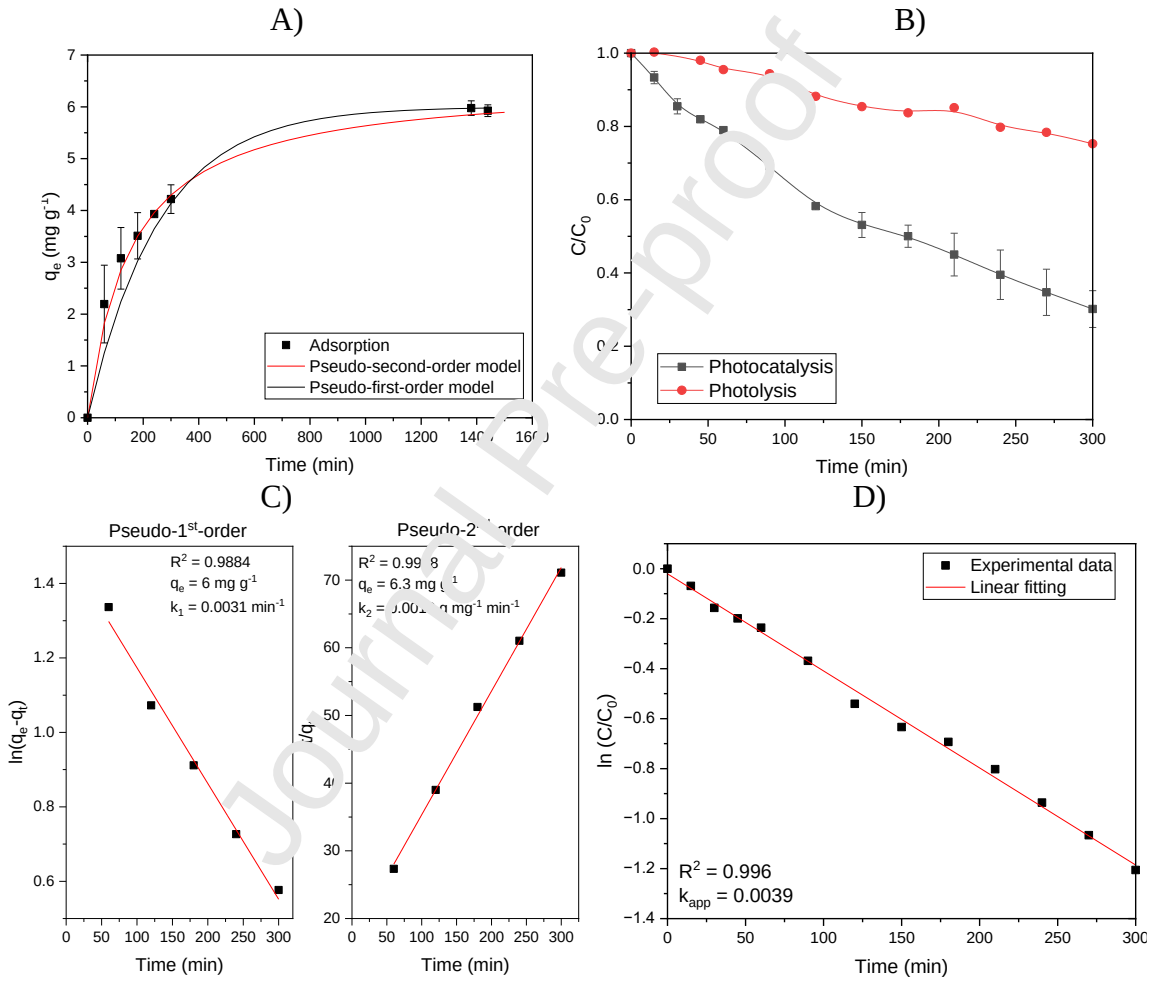

E)

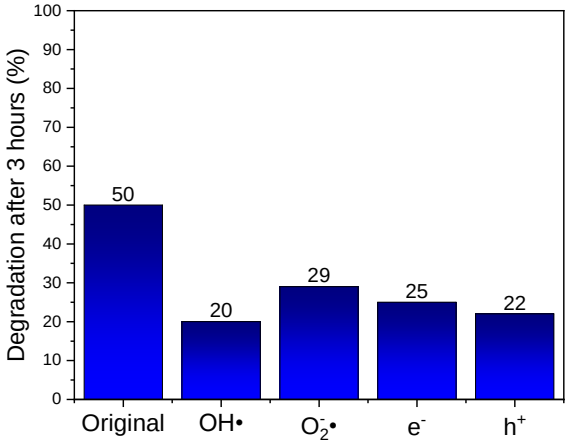

The results exhibited in Figure 13A show that 24 h is sufficient for the adsorption-desorption equilibrium to be achieved between the MB and the CB-Cat. Additionally, it is evident that CB-Cat indeed possesses photocatalytic activity, as the degradation of MB during the illumination period is much higher in the presence of the catalytic beads when compared to the photolysis test. Figure 13C demonstrates that the pseudo-second-order kinetic model is indeed more suitable to describe the adsorption process, as its R^2 is closer to 1 than the one obtained for the pseudo-first-order model. Figure 13D shows that the simplified Langmuir-Hinshelwood (L-H) kinetic model proposed previously can also be applied to this operational setting. Considering the pseudo-second-order adsorption model employed, it is possible to predict that nearly 20 h would be necessary to achieve 88% removal of the MB from the system through the simple adsorption process. Compared with the simultaneous adsorption/photocatalysis process, the same result was achieved after 5 h. Therefore, the illumination of the system with the simulated sunlight is undoubtedly advantageous for the removal of MB, rendering the simultaneous adsorption/photocatalysis process the optimal choice between processes evaluated in this study.

The mechanism of the MB photocatalytic degradation was evaluated through the scavenger methodology. Figure 13E illustrates that the predominant active radical accountable for the photodegradation of MB in heterogeneous photocatalysis is the hydroxyl radical. This inference is supported by the significant reduction in efficiency observed upon its suppression (from 50% to 20% removal after 3 hours). The inhibition of the superoxide active radical also led to decreased

degradation efficiency during the experiment, implying its contribution to the photodegradation process. Additionally, as suggested by the desorption results, a part of the adsorbed MB may undergo degradation through the direct photocatalysis mechanism, in which the electron holes are responsible for the degradation process. Based on these findings, we propose the subsequent mechanism to depict the generation of active radicals throughout the photocatalytic procedure. (Equations 9-14) [42]:

$$\text{CB-Cat} + \lambda \rightarrow e^- + h^+ \quad (9)$$

$$H_2O + h^+ \rightarrow {}^{\bullet}OH + H^+ \quad (10)$$

$$O_2 + e^- \rightarrow O_2^{\bullet -} \quad (11)$$

$${}^{\bullet}OH + {}^{\bullet}OH \rightarrow H_2O_2 \quad (12)$$

$$H_2O_2 + e^- \rightarrow {}^{\bullet}OH + OH^- \quad (13)$$

$$H_2O_2 + O_2^{\bullet -} \rightarrow {}^{\bullet}OH + O_2 + OH^- \quad (14)$$

Considering the results obtained for the mechanism of active radical generation, Figure 14 represents an overall schematization of the simultaneous adsorption/photocatalysis process studied in this work, employing the CB-Cat material.

Figure 14 – Schematization of the simultaneous adsorption-photocatalysis process

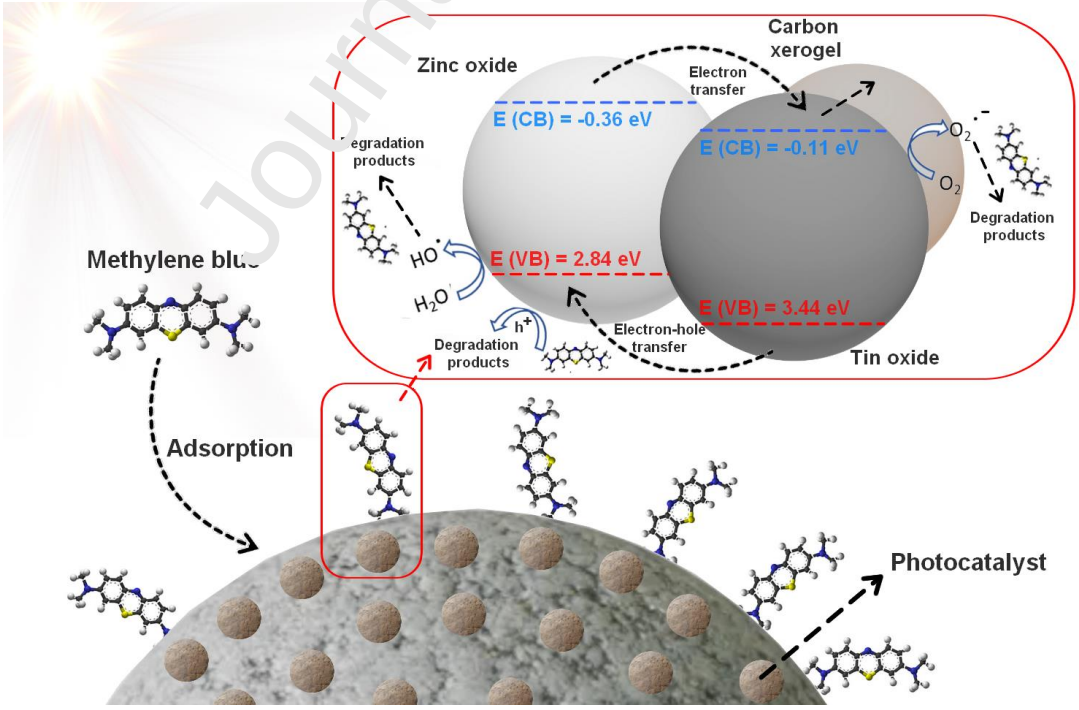

Taking into account the successful synergy presented by the hybrid process evaluated in this work toward the removal of methylene blue, the potential applications for the catalytic beads developed in this work are considerably diverse. Practical applications and future research prospects may involve the application of the CB-Cat in more complex systems (such as continuous reactors) and more complex organic molecules, such as persistent organic pollutants. In order to contextualize this work with related literature, Table 4 shows a comparison between various similar strategies employing cellulose beads to immobilize photocatalysts.

Photocatalyst	**Non-solvent**	**Type of light**	**Pollutant**	**% Removal**	**Reference**
ZnO/SnO_2/CX	NaCl	Simulated sunlight	Methylene blue	53% after 1h (25 ppm)	This work
Ag/AgCl	$AlCl_3$ and $FeCl_3$	Visible light	Rhodamine B	55% after 1h (25 ppm)	[43]
Fe(III) alginate-CMC	$FeCl_3$	Visible light	Malachite green	55% after 4h (10 ppm)	[44]
Au-doped TiO_2	NaCl	Visible light	Tylosin	43% after 1h (20 ppm)	[45]
TiO_2 nanowires	H_2SO_4	UV light	Methylene blue	55% after 400 min (10 ppm)	[46]

Conclusion

First, it is concluded that the synthesis proposed was successful in the incorporation of the proposed photocatalyst into the cellulose beads, as shown by the diverse characterization techniques employed, leading to its availability on the surface of the CB-Cat for the propagation of the heterogeneous photocatalysis process. Regarding the removal of methylene blue, the simultaneous adsorption/photocatalysis process was the superior option, as evidenced by the higher removal

efficiencies obtained, indicating that the synergy between the adsorption and photocatalysis processes can be efficiently harvested for the removal of organic pollutants in aqueous medium. Additionally, the regeneration of the photocatalytic beads between cycles was favorable in the context of MB removal, as this process helped to promote higher removal efficiencies after multiple cycles. Finally, it was determined that the photodegradation of the methylene blue was controlled by the formation of active radicals by the CB-Cat during the simulated sunlight irradiation, namely the hydroxyl and superoxide radicals.

Acknowledgments

The authors acknowledge the financial support provided by the São Paulo Research Foundation - FAPESP (Grants #2014/50945-4, #2017/10118-0, #2018/10492-1, #2018/16360-0 and #2022/04058-2) and National Council for Scientific and Technological Development - CNPq (Grants: #465571/2014-0 and #303943/2021-1).

References

[1] V.H. Nguyen, S.M. Smith, K. Wantala, P. Kajitvichyanukul, Photocatalytic remediation of persistent organic pollutants (POPs): A review, Arab. J. Chem. 13 (2020) 8309–8337. https://doi.org/10.1016/j.arabjc.2020.04.028.

[2] K. Ahmad, H.R. Ghatak, S.M. Ahuja, A review on photocatalytic remediation of environmental pollutants and H2 production through water splitting: A sustainable approach, Environ. Technol. Innov. 19 (2020) 100893. https://doi.org/10.1016/j.eti.2020.100893.

[3] O.D. Maynez-Navarro, J.L. Sánchez-Salas, Focus on Zinc Oxide as a Photocatalytic Material for Water Treatment, Int J Biorem Biodegrad. 106 (2018) 1–9. https://doi.org/10.29011/IJBB-106/100006.

[4] S. Wang, J.H. Yun, B. Luo, T. Butburee, P. Peerakiatkhajohn, S. Thaweesak, M. Xiao, L.

Wang, Recent Progress on Visible Light Responsive Heterojunctions for Photocatalytic Applications, J. Mater. Sci. Technol. 33 (2017) 1–22. https://doi.org/10.1016/j.jmst.2016.11.017.

[5] L. V. Bora, R.K. Mewada, Visible/solar light active photocatalysts for organic effluent treatment: Fundamentals, mechanisms and parametric review, Renew. Sustain. Energy Rev. 76 (2017) 1393–1421. https://doi.org/10.1016/J.RSER.2017.01.130.

[6] R. Nawaz, C.F. Kait, H.Y. Chia, M.H. Isa, L.W. Huei, N.T. Sahrin, N. Khan, Countering major challenges confronting photocatalytic technology for the remediation of treated palm oil mill effluent: A review, Environ. Technol. Innov. 23 (2021) 101764. https://doi.org/10.1016/J.ETI.2021.101764.

[7] P. Fernández-Ibáñez, J. Blanco, S. Malato, F.J. De Las Nieves, Application of the colloidal stability of TiO2 particles for recovery and reuse in solar photocatalysis, Water Res. 37 (2003) 3180–3188. https://doi.org/10.1016/S0043-1354(03)00157-X.

[8] S. Danfá, R.C. Martins, M.J. Quina, J. Gomes, Supported TiO2 in ceramic materials for the photocatalytic degradation of contaminants of emerging concern in liquid effluents: A review, Molecules. 26 (2021). https://doi.org/10.3390/molecules26175363.

[9] C. de Araújo Gusmão, P.H. Palharim, B. Ramos, A.C.S.C. Teixeira, Enhancing the visible-light photoactivity of silica-supported TiO2 for the photocatalytic treatment of pharmaceuticals in water, Environ. Sci. Pollut. Res. (2021). https://doi.org/10.1007/s11356-021-16718-w.

[10] S. Silvestri, M.G. Gonçalves, P.A. Da Silva Veiga, T.T.D.S. Matos, P. Peralta-Zamora, A.S. Mangrich, TiO 2 supported on Salvinia molesta biochar for heterogeneous photocatalytic degradation of Acid Orange 7 dye, J. Environ. Chem. Eng. 7 (2019) 102879. https://doi.org/10.1016/j.jece.2019.102879.

[11] Y. Chen, C. Shen, J. Wang, G. Xiao, G. Luo, Green Synthesis of Ag-TiO2 Supported on Porous Glass with Enhanced Photocatalytic Performance for Oxidative Desulfurization and Removal of Dyes under Visible Light, ACS Sustain. Chem. Eng. 6 (2018) 13276–13286. https://doi.org/10.1021/acssuschemeng.8b02860.

[12] A. Mishra, A. Mehta, S. Basu, Clay supported TiO2 nanoparticles for photocatalytic degradation of environmental pollutants: A review, J. Environ. Chem. Eng. 6 (2018) 6088–6107. https://doi.org/10.1016/j.jece.2018.09.029.

[13] K. Wu, B. Li, X. Dong, P. Wu, K. Sun, S. Yang, J. Wu, J. Hou, Z. Liu, X. Guo, Flexible And Recyclable PPy-TiO2@WO3 Photocatalyst Supported By Cellulose Aerogel Beads, ChemistrySelect. 5 (2020) 6527–6536. https://doi.org/10.1002/slct.202001045.

[14] J. Yang, X. Luo, Ag-doped TiO2 immobilized cellulose-derived carbon beads: One-Pot preparation, photocatalytic degradation performance and mechanism of ceftriaxone sodium, Appl. Surf. Sci. 542 (2021) 148724. https://doi.org/10.1016/j.apsusc.2020.148724.

[15] Z.H. Hu, A.M. Omer, X.K. Ouyang, D. Yu, Fabrication of carboxylated cellulose nanocrystal/sodium alginate hydrogel beads for adsorption of Pb(II) from aqueous solution, Int. J. Biol. Macromol. 108 (2018) 149–157. https://doi.org/10.1016/j.ijbiomac.2017.11.171.

[16] H. Zhao, X.K. Ouyang, L.Y. Yang, Adsorption of lead ions from aqueous solutions by porous cellulose nanofiber–sodium alginate hydrogel beads, J. Mol. Liq. 324 (2021) 115122. https://doi.org/10.1016/j.molliq.2020.115122.

[17] G. Cui, Y. Li, T. Shi, Z. Gao, N. Qiu, T. Satoh, T. Kakuchi, Q. Duan, Synthesis and characterization of Eu(III) complexes of modified cellulose and poly(N-isopropylacrylamide), Carbohydr. Polym. 94 (2013) 77–81. https://doi.org/10.1016/J.CARBPOL.2013.01.045.

[18] M. Gericke, J. Trygg, P. Fardim, Functional cellulose beads: Preparation, characterization, and applications, Chem. Rev. 113 (2013) 4812–4836. https://doi.org/10.1021/cr300242j.

[19] D. Yang, Y. Wang, C. Chen, Y. Su, L. Li, L. Miao, H. Gu, W. Zhao, L. Ding, D. Hu, Oriented Plate-like KNbO3 Polycrystals: Topochemical Mesocrystal Conversion and Piezoelectric and Photocatalytic Responses, Inorg. Chem. 62 (2023) 10408–10419. https://doi.org/10.1021/ACS.INORGCHEM.3C01286/ASSET/IMAGES/LARGE/IC3C01286_0015.JPEG.

[20] N.P. de Moraes, C.M. Goes, D.C. Sperandio, R. da S. Rocha, R. Landers, T. Paramasivam, L.A. Rodrigues, Development of a new zinc oxide/tin oxide/carbon xerogel photocatalyst for visible light photodegradation of 4-chlorophenol, Mater. Sci. Eng. B Solid-State Mater. Adv. Technol. 269 (2021) 115183. https://doi.org/10.1016/j.mseb.2021.115183.

[21] B. Medronho, B. Lindman, Brief overview on cellulose dissolution/regeneration interactions and mechanisms, Adv. Colloid Interface Sci. 222 (2015) 502–508. https://doi.org/10.1016/j.cis.2014.05.004.

[22] N.P. de Moraes, R.B. Valim, R. da Silva Rocha, M.L.C.P. da Silva, T.M.B. Campos, G.P. Thim, L.A. Rodrigues, Effect of synthesis medium on structural and photocatalytic properties of ZnO/carbon xerogel composites for solar and visible light degradation of 4-chlorophenol and bisphenol A, Colloids Surfaces A Physicochem. Eng. Asp. 584 (2020) 124034. https://doi.org/10.1016/j.colsurfa.2019.124034.

[23] N.P. de Moraes, L.A. Bacetto, G.S. dos Santos, M.L.C. Pinto da Silva, J.P.B. Machado, T.M.B. Campos, G.P. Thim, L.A. Rodrigues, Synthesis of novel ZnO/carbon xerogel composites: Effect of carbon content and calcination temperature on their structural and photocatalytic properties, Ceram. Int. 45 (2019) 3657–3667. https://doi.org/10.1016/j.ceramint.2018.11.027.

[24] N.P. de Moraes, F.A. Torezin, G.V. Jucá Dantas, J.G.M. de Sousa, R.B. Valim, R. da Silva Rocha, R. Landers, M.L.C.P. da Silva, L.A. Rodrigues, TiO2/Nb2O5/carbon xerogel ternary photocatalyst for efficient degradation of 4-chlorophenol under solar light irradiation, Ceram. Int. 46 (2020) 14505–14515. https://doi.org/10.1016/j.ceramint.2020.02.249.

[25] S. Shankar, J.W. Rhim, Preparation of nanocellulose from micro-crystalline cellulose: The effect on the performance and properties of agar-based composite films, Carbohydr. Polym. 135 (2016) 18–26. https://doi.org/10.1016/j.carbpol.2015.08.082.

[26] N.P. de Moraes, R. Bacani, M.L.C.P. da Silva, T.M.B. Campos, G.P. Thim, L.A. Rodrigues, Effect of Nb/C ratio in the morphological, structural, optical and photocatalytic properties of novel and inexpensive Nb2O5/carbon xerogel composites, Ceram. Int. 44 (2018) 6645–6652. https://doi.org/10.1016/j.ceramint.2018.01.070.

[27] X. Feng, B. Wang, G. Gao, S. Gao, C. Xie, J.W. Shi, MnyCo3−yOx bimetallic oxide prepared by ultrasonic technology for significantly improved catalytic performance in the reduction of NOx with NH3, Fuel. 352 (2023) 129159. https://doi.org/10.1016/J.FUEL.2023.129159.

[28] Y. Zheng, Y. Liu, X. Guo, Z. Chen, W. Zhang, Y. Wang, X. Tang, Y. Zhang, Y. Zhao, Sulfur-doped g-C3N4/rGO porous nanosheets for highly efficient photocatalytic degradation of refractory contaminants, J. Mater. Sci. Technol. 41 (2020) 117–126. https://doi.org/10.1016/J.JMST.2019.09.018.

[29] I. Khan, K. Saeed, I. Zekker, B. Zhang, A.H. Hendi, A. Ahmad, S. Ahmad, N. Zada, H. Ahmad, L.A. Shah, T. Shah, I. Khan, Review on Methylene Blue: Its Properties, Uses, Toxicity and Photodegradation, Water (Switzerland). 14 (2022). https://doi.org/10.3390/w14020242.

[30] N.P. de Moraes, A. de Siervo, T.O. Silva, R. da Silva Rocha, D.A. Reddy, Y. Lianqing, M.R. de Vasconcelos Lanza, L.A. Rodrigues, Kraft lignin-based carbon xerogel/zinc oxide

composite for 4-chlorophenol solar-light photocatalytic degradation: effect of pH, salinity, and simultaneous Cr(VI) reduction, Environ. Sci. Pollut. Res. (2022). https://doi.org/10.1007/s11356-022-22825-z.

[31] R.L. Oliveira, J.G. Vieira, H.S. Barud, R.M.N. Assunção, G.R. Filho, S.J.L. Ribeiro, Y. Messadeqq, Synthesis and characterization of methylcellulose produced from bacterial cellulose under heterogeneous condition, J. Braz. Chem. Soc. 26 (2015) 1861–1870. https://doi.org/10.5935/0103-5053.20150163.

[32] N. Atykyan, V. Revin, V. Shutova, Raman and FT-IR Spectroscopy investigation the cellulose structural differences from bacteria Gluconacetobacter sucrofermentans during the different regimes of cultivation on a molasses media, AMB Express. 10 (2020). https://doi.org/10.1186/s13568-020-01020-3.

[33] N. Perciani de Moraes, R. da Silva Rocha, M.L. Caetano Pinto da Silva, T.M. Bastos Campos, G.P. Thim, R. Landers, L.A. Rodrigues, Facile preparation of Bi-doped ZnO/β-Bi2O3/Carbon xerogel composites towards visible-light photocatalytic applications: Effect of calcination temperature and bismuth content, Ceram. Int. 46 (2020) 23895–23909. https://doi.org/10.1016/j.ceramint.2020.06.166.

[34] S.G. Kumar, K.S.R.K. Rao, Zinc oxide based photocatalysis: Tailoring surface-bulk structure and related interfacial charge carrier dynamics for better environmental applications, RSC Adv. 5 (2015) 3306–3351. https://doi.org/10.1039/c4ra13299h.

[35] W.Z. Durrani, A. Nasrullah, A.S. Khan, T.M. Fagieh, E.M. Bakhsh, K. Akhtar, S.B. Khan, I.U. Din, M.A. Khan, A. Bokhari, Adsorption efficiency of date palm based activated carbon-alginate membrane for methylene blue, Chemosphere. 302 (2022) 134793. https://doi.org/10.1016/J.CHEMOSPHERE.2022.134793.

[36] L.A. Rodrigues, M.L.C.P. da Silva, Thermodynamic and kinetic investigations of phosphate

adsorption onto hydrous niobium oxide prepared by homogeneous solution method, Desalination. 263 (2010) 29–35. https://doi.org/10.1016/j.desal.2010.06.030.

[37] L.A. de Sousa Ribeiro, G.P. Thim, M.O. Alvarez-Mendez, A. dos Reis Coutinho, N.P. de Moraes, L.A. Rodrigues, Preparation, characterization, and application of low-cost açaí seed-based activated carbon for phenol adsorption, Int. J. Environ. Res. 12 (2018) 755–764. https://doi.org/10.1007/s41742-018-0128-5.

[38] S. Kalam, S.A. Abu-Khamsin, M.S. Kamal, S. Patil, Surfactant Adsorption Isotherms: A Review, ACS Omega. 6 (2021) 32342–32348. https://doi.org/10.1021/acsomega.1c04661.

[39] X. Chen, X. Liu, L. Zhu, X. Tao, X. Wang, One-step fabrication of novel MIL-53(Fe, Al) for synergistic adsorption-photocatalytic degradation of tetracycline, Chemosphere. 291 (2022). https://doi.org/10.1016/j.chemosphere.2021.133032.

[40] L.A. Rodrigues, M.L.C.P. Da Silva, Adsorption of phosphate ions on hydrous niobium oxide, Quim. Nova. 32 (2009) 1206–1211. https://doi.org/10.1590/S0100-40422009000500023.

[41] X. Zhang, T. Peng, S. Song, Recent advances in dye-sensitized semiconductor systems for photocatalytic hydrogen production, J. Mater. Chem. A. 4 (2016) 2365–2402. https://doi.org/10.1039/C5TA08939E.

[42] N.P. de Moraes, G.S. dos Santos, G.C. Neves, R.B. Valim, R. da Silva Rocha, R. Landers, M.L. Caetano Pinto da Silva, L.A. Rodrigues, Development of Nb2O5-doped ZnO/Carbon xerogel photocatalyst for the photodegradation of 4-chlorophenol, Optik (Stuttg). 219 (2020). https://doi.org/10.1016/j.ijleo.2020.165238.

[43] H. Heidarpour, M. Golizadeh, M. Padervand, A. Karimi, M. Vossoughi, M.H. Tavakoli, In-situ formation and entrapment of Ag/AgCl photocatalyst inside cross-linked carboxymethyl cellulose beads: A novel photoactive hydrogel for visible-light-induced photocatalysis, J.

Photochem. Photobiol. A Chem. 398 (2020) 112559. https://doi.org/10.1016/j.jphotochem.2020.112559.

[44] D. Karadeniz, N. Kahya, F.B. Erim, Effective photocatalytic degradation of malachite green dye by Fe(III)-Cross-linked Alginate-Carboxymethyl cellulose composites, J. Photochem. Photobiol. A Chem. 428 (2022) 113867. https://doi.org/10.1016/j.jphotochem.2022.113867.

[45] P. Zhao, Y. Yang, Y. Pei, X. Luo, TEMPO-oxidized cellulose beads embedded with Au-doped TiO2 nanoparticles for photocatalytic degradation of Tylosin, Cellulose. 30 (2023) 1133–1147. https://doi.org/10.1007/s10570-022-04935-6.

[46] C.Y.Y. Evyan, K.M. Salleh, M.Y. Chong, C.H. Chia, S. Zakaria, Effect of dimensionality of nanosized TiO2 embedded in regenerated cellulose beads as a portable catalyst for reusable decomposition system, Polym. Adv. Technol. 32 (2021) 3549–3562. https://doi.org/10.1002/pat.5365.

Credit author statement

Nicolas Perciani de Moraes: Formal analysis; Investigation; Methodology; Software; Validation; Visualization; Roles/Writing - original draft; Writing - review & editing.

Renan Amarante Pereira: Formal analysis; Investigation; Methodology; Validation; Software; Visualization; Roles/Writing - original draft.

Thiago Vieira Chicuta da Silva: Formal analysis; Investigation; Methodology; Validation; Software; Visualization; Roles/Writing - original draft.

Bruno Henrique Baena da Silva: Formal analysis; Investigation; Methodology; Validation; Software; Visualization; Roles/Writing - original draft.

Gabrielle Policarpo de Assis: Formal analysis; Investigation; Methodology; Validation; Software; Visualization; Roles/Writing - original draft.

Tiago Moreira Bastos Campos: Formal analysis; Investigation; Methodology; Validation; Software; Visualization; Roles/Writing - original draft.

Gilmar Patrocinio Thim: Formal analysis; Funding acquisition; Investigation; Methodology; Validation; Software; Visualization; Roles/Writing - original draft.

Marcos Roberto de Vasconcelos Lanza: Formal analysis; Funding acquisition; Investigation; Methodology; Project administration; Software; Supervision; Validation; Visualization; Roles/Writing - original draft; Writing - review & editing

Larissa de Freitas: Formal analysis; Funding acquisition; Investigation; Methodology; Project administration; Software; Supervision; Validation; Visualization; Roles/Writing - original draft; Writing - review & editing

Liana Alvares Rodrigues: Formal analysis; Funding acquisition; Investigation; Methodology; Project administration; Software; Supervision; Validation; Visualization; Roles/Writing - original draft; Writing - review & editing.

Declaration of interests

☒ The authors declare that they have no known competing financial interests or personal relationships that could have appeared to influence the work reported in this paper.

☐The authors declare the following financial interests/personal relationships which may be considered as potential competing interests: